Journal of ELECTRONIC MATERIALS, Vol. 47, No. 8, 2018
https://doi.org/10.1007/s11664-018-6363-x

Theoretical and Field Experimental Investigation of an Arrayed Solar Thermoelectric Flat-Plate Generator

NAVEED UR REHMAN[1,2] and MUBASHIR ALI SIDDIQUI[1]

1.—Solar Energy Lab, Mechanical Engineering Department, NED University of Engineering and Technology, University Road, Karachi 75270, Pakistan. 2.—e-mail: naveedurrehman@neduet.edu.pk

This work theoretically and experimentally investigated the performance of an arrayed solar flat-plate thermoelectric generator (ASFTEG). An analytical model, based on energy balances, was established for determining load voltage, power output and overall efficiency of ASFTEGs. An array consists of TEG devices (or modules) connected electrically in series and operating in closed-circuit mode with a load. The model takes into account the distinct temperature difference across each module, which is a major feature of this model. Parasitic losses have also been included in the model for realistic results. With the given set of simulation parameters, an ASFTEG consisting of four commercially available Bi_2Te_3 modules had a predicted load voltage of 200 mV and generated 3546 μW of electric power output. Predictions from the model were in good agreement with field experimental outcomes from a prototype ASFTEG, which was developed for validation purposes. Later, the model was simulated to maximize the performance of the ASFTEG by adjusting the thermal and electrical design of the system. Optimum values of design parameters were evaluated and discussed in detail. Beyond the current limitations associated with improvements in thermoelectric materials, this study will eventually lead to the successful development of portable roof-top renewable TEGs.

Key words: Multi-module thermoelectric, arrayed thermoelectric, thermoelectric generator, parasitic loss, flat-plate solar, flat-panel thermoelectric, non-concentrating solar

INTRODUCTION

Solar energy is renewable, green and abundant, but harnessing it effectively requires considerable effort.[1] To date, several devices have been developed for converting solar energy into electricity. Currently, the application of thermoelectric generator (TEG) devices for converting solar energy into electricity is receiving significant attention.[2–5] The commercial version of these devices (hereafter called "modules") consists of thermoelectric material sandwiched between substrate plates (Fig. 1). The thermoelectric material consists of several thermocouples, joined electrically in series. The legs (or thermopiles) of these thermocouples are made up of *p*- and *n*-type electronic materials to boost the thermal-to-electric conversion phenomenon, also called the Seebeck effect.[6] The substrate plates are usually ceramics, which are electrically insulating but have high thermal conductivity. All the connected thermocouples are placed between these plates so that they are thermally in parallel with each other. When heat is supplied to one plate (the "hot side") of the module, it travels to the other plate (the "cold side") creating a temperature difference across the module. This temperature difference causes every thermocouple to produce an electric potential across its legs. Due to the large number of thermocouples, the generated electrical potential is

(Received December 26, 2017; accepted May 5, 2018; published online May 17, 2018)

additive. So far, the discussed electric circuit is operating with no electric load; this is referred to as open-circuit mode. If a load (or electric resistance) is attached to a circuit so that it is connected with one leg of the first thermocouple and the other leg of the last thermocouple, an electric current will start flowing; this is called closed-circuit mode. Current flow results in a power output that drives the load (e.g. fan, bulb, or other electrically operated device). The thermal-to-electrical conversion efficiency is the ratio of power output-to-the rate of heat supply at the hot side. Being solid-state devices, these modules have several advantages, including silent operation because of the absence of any moving parts, modularity in design, and good reliability.

In a solar TEG (STEG), modules are operated with solar energy as the input on the hot side. These generators transform solar energy directly into electricity, without the use of conventional ancillaries such as boilers, turbines or engines. Although an STEG is a heat-operated device, its use can be extended for operation at night or when solar radiation levels are low using auxiliary fuels. This can be done by coupling an STEG with, for example, a thermal storage system[7] or engine exhaust.[8]

To date, STEGs are suitable for power generation at micro-scales since they have low conversion efficiencies, which are currently severely constrained by existing research in the field of material sciences and engineering.[9] As a result, two approaches can be used to increase power output from STEGs: (1) using optical concentrators; and (2) adopting methods that minimize thermal losses. The former approach yields high solar intensities, resulting in high power outputs per module. However, the use of large concentrator devices (e.g. linear parabolic troughs,[10] paraboloidal dishes[11] and Fresnel lenses[12]) makes the system bulkier and requires sophisticated sun-tracking mechanisms, which may be difficult for domestic consumers to handle.[13] The latter approach aims to achieve useful gains from available solar radiation using selective paints on the hot side of modules to increase solar absorption, and air evacuation for suppressing convection losses. STEGs can also be used with a flat-plate collector (solar flat-plate TEGs or SFTEGs). Although the efficiencies of SFTEGs are comparatively low, they offer two key advantages over concentrated systems. First, they are compact and can be built in portable and roof-top designs. Second, they do not require complex sun-tracking mechanisms.

It is obvious that obtaining substantial power output from an SFTEG to drive even small equipment would require a number of modules connected electrically in series. Such a setup is referred to as an arrayed SFTEG (ASFTEG). However, most studies to date have used designs with single modules only. For example, Goldsmith et al.[14] performed experimental studies with a commercial module consisting of 31 thermocouples. Omer and Infield[15] proposed a theoretical model using a single module, while experiments were performed using a module with 127 thermocouples. Lenoir et al.[16] developed an analytical model and simulated it with a module composed of 539 thermocouples. The reason for modeling and performing experiments with a single TEG may be the assumption that output in an arrayed configuration (comprising several modules) would simply be the combination of the outputs from single modules. However, that may not be case since modules arranged in series would have dissimilar temperature differences. This temperature mismatch is a natural phenomenon and can occur even in steady-state operation. Reasons may include inherent variation in properties, parasitic losses, rise in temperature of the convection fluid, or thermal bridges inside SFTEGs, which may also lead to spatial variations of temperature inside the collector. Recently, Montecucco et al.[17] established a model and performed experiments to quantify the effects of temperature mismatch in

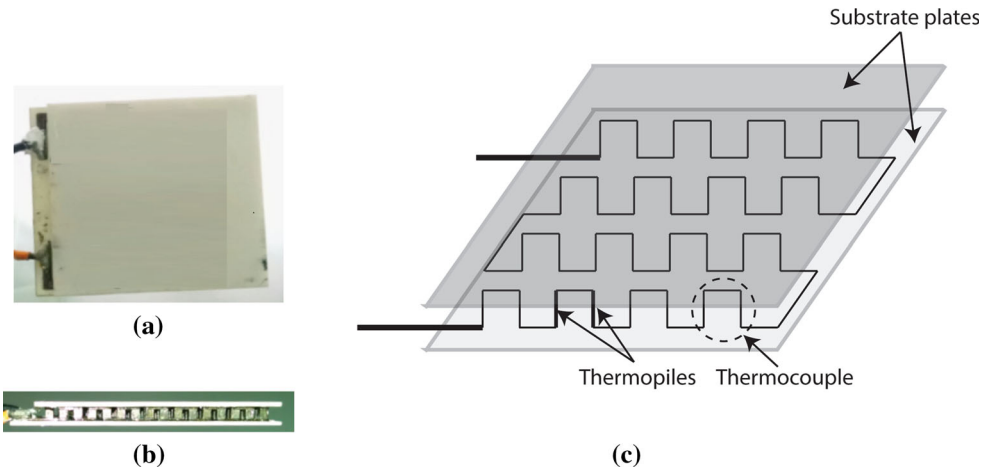

Fig. 1. Thermoelectric generator module: (a) top, (b) side, and (c) schematic views.

different electrical configurations, but the study did not involve SFTEGs. Their proposed model was based on the hypothesis that the temperature differences across module surfaces are constant and the experiments were performed in a laboratory setup with a dedicated heat source and sink that could maintain the desired temperatures across modules. However, the outputs predicted from such models may deviate from reality since the temperature differences would in fact be based upon thermal loadings from solar energy and associated energy losses. In other words, in the case of solar-based applications, performance modeling approaches that are based on energy balances are more realistic. Some efforts were made by Vargas-Almeida et al.[18,19] to analyze the impact of different electrical configurations on performance, but, again, the proposed models were not compatible with assessing yields from SFTEGs.

In the literature, most of the attempts at modeling thermoelectric generation have paid little or no attention to the interior of the modules, which may contribute to parasitic losses, thus diminishing performance. Inherently, there are two types of parasitic resistances associated with a physical module: (1) parasitic thermal resistance (PTR), which may be attributed to substrate materials and overhanging in electrical connections between thermopiles, reducing the temperature difference across the thermoelectric material; and (2) parasitic electrical resistance (PER), which may be attributed to contact resistances and improper soldering that drops the voltage before the electric load. Recently, Hsu et al.[20] emphasized this point and reported the actual Seebeck coefficient of a chosen module to be around 87% of the thermoelectric material. Ebling et al.[21] reported substantial drops in figures of merit due to PER using multiphysics simulations. Apertet et al.[22] concluded that the intrinsic characteristics of thermoelectric materials would be of little interest in performance improvement and that thermal impedances and electric load matching should be considered for maximizing outputs. Surprisingly, very few studies have been found that account for these parasitic losses in conjunction with STEGs.[9]

Based on the above discussion, establishing a model that accounts for temperature mismatches in an array of modules for predicting output and overall solar-to-electric conversion efficiency in ASFTEGs would be a significant contribution. The modeling approach should incorporate energy balances that account for solar radiation and energy losses, rather than temperature differences across the module. Including parasitic resistances makes it a more realistic model. This work aimed to establish an analytical model with these features and conduct an experimental validation. The model was also simulated to optimize the thermal and electrical design of an ASFTEG.

THEORETICAL MODEL

In this section, a detailed analytical model of an ASFTEG is developed. As discussed, an ASFTEG consists of an array of modules electrically connected in series with a load, as shown in Fig. 2.

Taking into account the thermoelectric properties, a single module can generate maximum voltage (υ_o, V) in open-circuit mode:

$$\upsilon_o = S_{mat}\Delta T_{mat} \tag{1}$$

where S_{mat} (V/K) is the Seebeck coefficient and $\Delta T_{mat} = T_{mat,h} - T_{mat,c}$ (K) is the temperature difference. Both the Seebeck coefficient and the temperature difference are associated with the thermoelectric material, not the module.

In an ASFTEG consisting of 'ξ' number of modules, the total maximum voltage (V_o, V) in open-circuit mode is the sum of the voltages of all individual modules in the array:

$$V_o = \sum_{m=1}^{\xi} \upsilon_{om} = S_{mat} \sum_{m=1}^{\xi} \Delta T_{matm} \tag{2}$$

where 'm' above and hereafter represents a property associated with the mth module in the circuit. It is assumed that the thermoelectric material inside all modules has the same Seebeck coefficient.

In Eq. 2, if an equal temperature difference is considered across each material ($= \Delta T_{mat}$), the summation sign is replaced by ξ. However, as discussed in the "Introduction", this would be an unrealistic assumption. These temperature differences are, therefore, measured individually, which is a major feature of this model.

In closed-circuit mode, the voltage (V_L, V) generated at load (R_L, Ω) is less than the open-circuit voltage because of the internal resistance of the thermoelectric materials inside the module:

$$V_L = V_o - I\left(\xi \cdot R_{el,mat}\right) \tag{3}$$

where I (A) is the current flowing through the circuit and $R_{el,mat}$ (Ω) is the internal resistance of a single module, taken as a constant for every module in the array.

In any closed electric circuit, current flow is a dependent property, which relies on the voltage source and electric resistances. For the circuit shown in Fig. 2b, the current can be estimated using Ohm's law as:

$$I = V_o / \left(\xi \cdot R_{el,mat} + R_L\right) \tag{4}$$

Substituting Eqs. 2 and 4 in Eq. 3 and simplifying, we get:

$$V_L = S_{mat}\left(\frac{M}{M+n}\right) \sum_{m=1}^{\xi} \Delta T_{mat\,m} \tag{5}$$

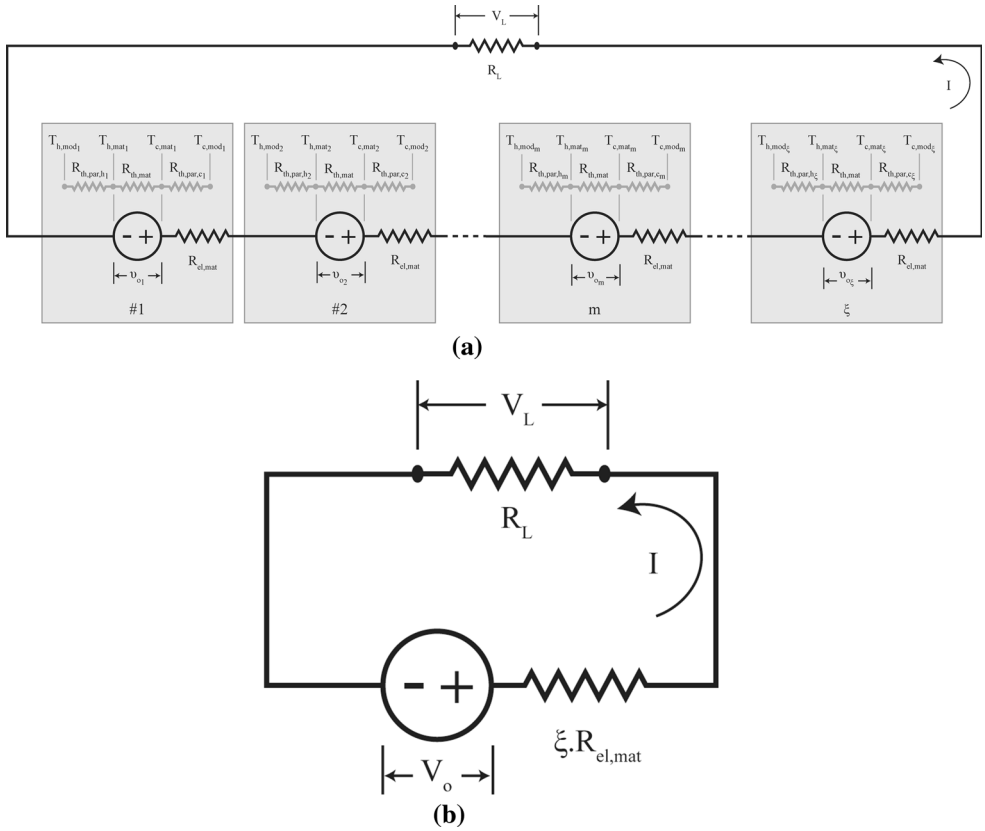

Fig. 2. (a) An electrical circuit for an arrayed solar flat-plate thermoelectric generator is shown. Each module can be viewed as a combination of a voltage source and an internal electric resistance of thermoelectric material. The voltage generated by a module depends upon the temperature difference across it. All modules are connected electrically in series with a load, shown by electric resistance. A thermal circuit consisting of parasitic thermal resistances at the hot and cold side is also shown beside each module. (b) This figure shows an equivalent electrical circuit diagram in which all voltage sources and internal electric resistances are summed into a single voltage source (V_o) and a resistor ($\xi R_{el,mat}$).

where M is the matched electric load, defined as the ratio of electric load-to-the internal resistance of a single module:

$$M = R_L/R_{el,mat} \tag{6}$$

Equation 5 is an important relationship, which will later be used for calculating the power output and overall conversion efficiency of the ASFTEG. Evaluating the load voltage from this equation requires measurement of the temperature difference directly across the thermoelectric material, which is difficult since commercial modules have their thermoelectric material tightly adhered between two thin substrate plates. Removing these substrates for plugging in temperature sensors can damage the module. An appropriate solution to this problem requires transforming ΔT_{mat} into ΔT_{mod} and using energy balances, where the latter is the temperature difference across the module surfaces.

The flow of energy through the thermal circuit of a module consists primarily of incident solar energy and thermal losses at the hot side, conversion of useful solar energy gain into electric energy and finally, heat rejection at the cold side of the module, as shown in Fig. 3. Incident solar radiation reaches the hot side of the module, where part of it is lost to the surroundings due to conduction, convection and radiation losses. Useful solar heat energy gain flows from the surface, through the parasitic thermal resistances at the hot side to the thermoelectric material. Within the thermoelectric material, conduction, the Seebeck effect and Joule's heating all contribute to its transfer. On application of an electric load, part of this energy is converted into electric energy. This conversion will depend upon not only the temperature difference across the thermoelectric material, but also the Seebeck coefficient and electric load (not shown in this figure). The remaining unconverted part of the energy is transferred from the cold side of the thermoelectric material through parasitic thermal resistance to the surroundings. Convective heat transfer pumps waste heat from the cold side.

A module receives heat from incident solar energy, and while part of it is lost to the surroundings due to conduction, convection and radiation losses, a useful energy gain flows through the module:

$$Q_{hm} = A\left[G - U_{loss}\left(T_{h,mod\,m} - T_a\right)\right] \tag{7}$$

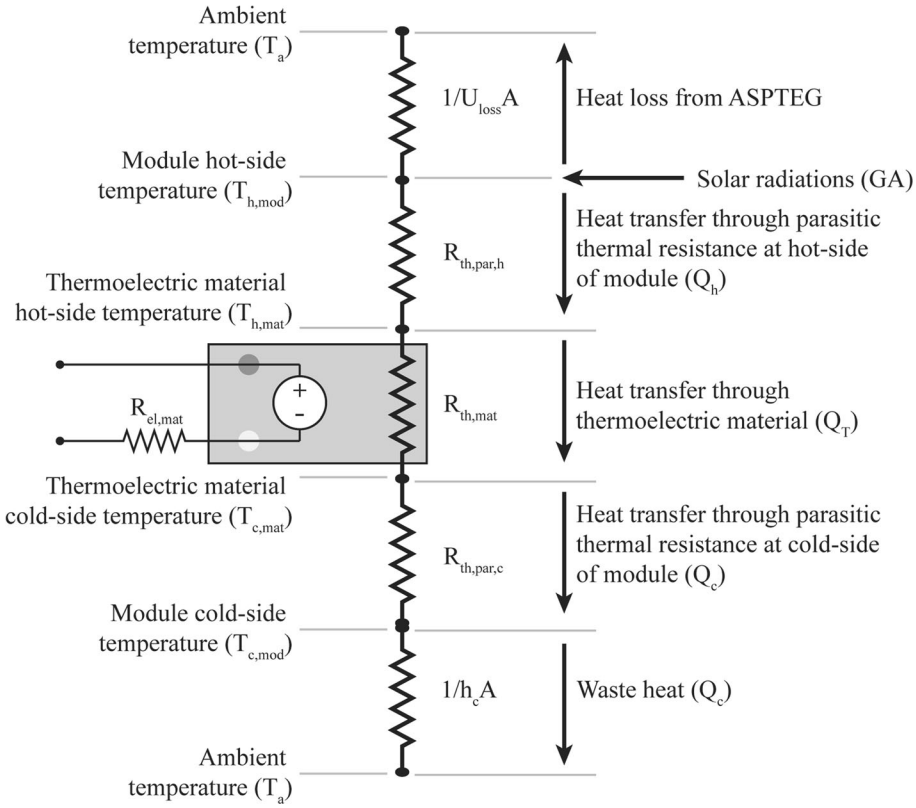

Fig. 3. Energy balance for a single module inside an arrayed solar flat-plate thermoelectric generator.

where Q_{hm} (W) is the useful solar energy gain in the form of heat accumulated at the hot side of the module, A (m^2) is the surface area of the module, G (W/m^2) is the incident solar intensity, U_{loss} (W/m^2 K) is the overall heat loss coefficient from ASFTEG, $T_{h,mod}$, (K) is the module hot-side temperature, and T_a (K) is the ambient temperature.

The temperature at the hot side of the thermoelectric material ($T_{h,mat}$, K) is less than the module surface temperature due to PTR ($R_{th,par,h}$, K/W) at the hot side:

$$T_{h,mat\,m} = T_{h,mod\,m} - Q_{hm}R_{th,par,hm} \tag{8}$$

In the above, the PTR can be different for each module, which is certainly a realistic assumption, as discussed in the "Introduction".

The accumulated heat is transferred from the hot side to the cold side of the module, while part of it is converted into electricity. This flow of energy through the module (Q_T, W) is not only attributed to heat conduction but to the Seebeck effect and Joule heating as well. Any of the following relationships can be used in this regard:

$$Q_{Tm} = \begin{cases} Q_{hm} = S_{mat}T_{h,matm}I + \frac{(T_{h,mat\,m} - T_{c,matm})}{R_{th,mat}} - \frac{1}{2}I^2R_{el,mat} \\ Q_{cm} = S_{mat}T_{c,mat\,m}I + \frac{(T_{h,matm} - T_{c,matm})}{R_{th,mat}} + \frac{1}{2}I^2R_{el,mat} \end{cases} \tag{9}$$

The remaining unconverted part of the heat is rejected as waste energy (Q_c, W). Transferring this energy out of the module is essential or it will increase the cold-side temperature, which is undesirable. If it is accomplished by convection, the following equation can be used:

$$Q_{cm} = h_cA\left(T_{c,modm} - T_a\right) \tag{10}$$

where h_c (W/m^2 K) is the convection coefficient and $T_{c,mod}$ (K) is the temperature, both at the cold side of the module. If convection is assisted by wind, the McAdams equation[23] can be used to determine the convection coefficient, based on average wind speed (V_w, m/s):

$$h_c = h_w = 5.7 + 3.8 \times V_w \tag{11}$$

Again, due to PTR at the cold side ($R_{th,par,c}$, K/W), the temperature at the thermoelectric material will be higher than module's surface temperature, such that:

$$T_{c,mat\,m} = T_{c,modm} + Q_{cm}R_{th,par,cm} \tag{12}$$

Finally, total electric power output (P, W) and overall solar-to-electric conversion efficiency (η) can be obtained by:

$$P = I \cdot V_L \tag{13}$$

and

$$\eta = P/(G\xi A) \tag{14}$$

In general, the specifications for commercial modules do not contain values for PTR. A methodology for evaluating the PTR is therefore presented here. Consider the operation of a single module in open-circuit mode, as shown in Fig. 4. Heat is absorbed at the hot side, passes through the module, and leaves from the cold side. This heat transfer is due to thermal conduction only. Also, as there is no load connected, no power output is generated.

As there is no load connected to the module, all the heat absorbed at the hot side will be transferred to the cold side by thermal conduction only. The following equality of thermal energies holds in open-circuit mode only:

$$Q = Q_h = Q_T = Q_c \tag{15}$$

Heat transfer due to conduction is directly proportional to the temperature difference across two surfaces and inversely proportionally to the thermal resistances that exist between these surfaces[24]:

$$\frac{T_{h,mat} - T_{c,mat}}{R_{th,mat}} = \frac{T_{h,mod} - T_{c,mod}}{R_{th,par,h} + R_{th,mat} + R_{th,par,c}} \tag{16}$$

The above equation gives an interesting relationship between the temperature differences across the material and the module. Using this relationship in Eq. 1 and assuming that hot-side and cold-side parasitic thermal resistances are equal ($R_{th,par} = R_{th,par,h} = R_{th,par,c}$):

$$\upsilon_o = S_{mat}\left[\frac{R_{th,mat}}{2 \cdot R_{th,par} + R_{th,mat}}\right]\Delta T_{mod} \tag{17}$$

The above equation can be used to experimentally evaluate PTR when material properties (Seebeck coefficient and thermal resistance of the thermoelectric material), the temperature difference across the module surfaces, and open-circuit voltages are known. Note that this does not require any knowledge about the amount of heat transferred through the module.

ARRAYED SOLAR FLAT-PLATE THERMOELECTRIC GENERATOR

Figure 5 shows a schematic of an ASFTEG prototype fabricated for the experimental validation of the established model. It consists of a double-walled air-tight box with a closed chamber inside. Acrylic was chosen for the box material because of its high solar transmittance (0.8) and low absorptivity (0.08).[25] Compared with ordinary glass, acrylic is lightweight and impact-resistant. The walls, mounting plate, stands and base were all cut from a 4-mm-thick acrylic plastic sheet using a commercial-scale laser cutting machine. These pieces were fastened together by applying super-glue at the mating edges. Four commercially available modules (same brand and model) were mounted on a mounting plate, which was placed inside the chamber so that the hot side of each module was inside the chamber and the cold side was open to the environment. The hot sides and inside of the mounting plate were coated with black paint to enhance solar absorptivity. Table I lists the technical specifications of the chosen module.

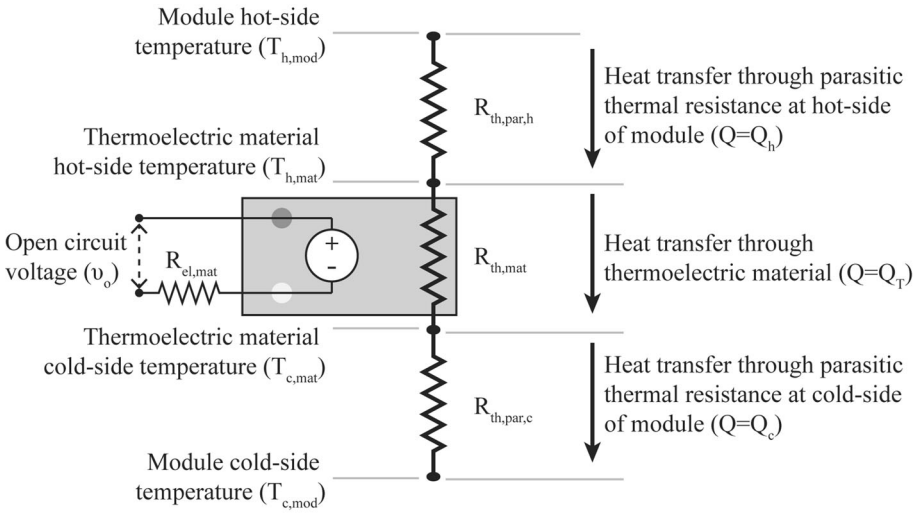

Fig. 4. Operation of a module in open-circuit mode.

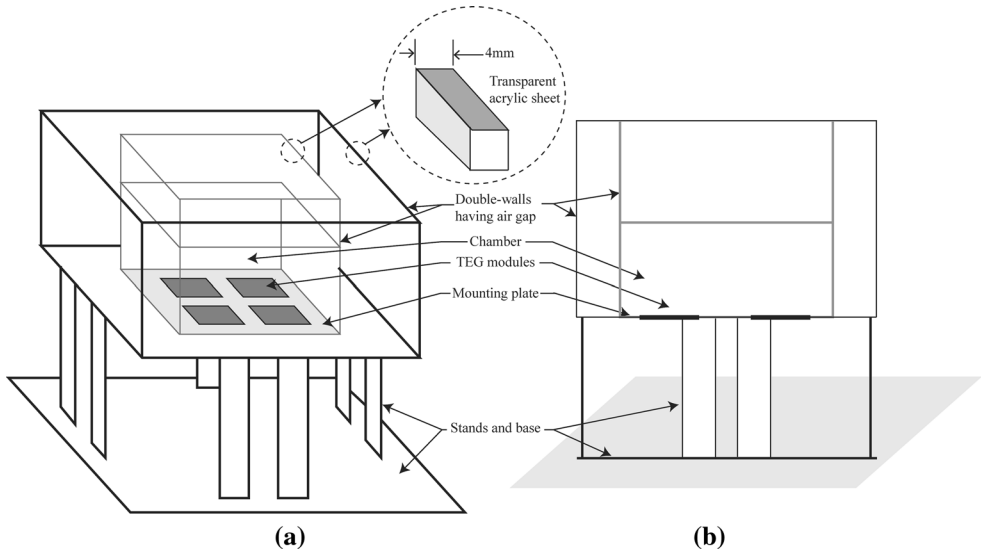

Fig. 5. (a) Axonometric and (b) orthogonal views of arrayed solar flat-plate thermoelectric generator (schematic).

Table I. Technical specifications of a commercially available Bi_2Te_3-based thermoelectric generator module used in the arrayed solar flat-plate thermoelectric generator prototype

Parameters	Specifications
Module	
Thermoelectric material	Bi_2Te_3
Substrate material	Alumina (Al_2O_3)
Length × width × height	40 mm × 40 mm × 3.6 mm
Thermoelectric leg (or thermopile)	
Height (h_{leg})	1.6 mm
Area (A_{leg})	$1.82mm^2$
Geometric ratio (G_{leg})	$A_{leg}/h_{leg} = 1.1375$mm
Seebeck coefficient (S_{leg})	210μV/K
Thermal conductivity (K_{leg})	1.55×10^{-2}W/cm K
Electrical resistivity (R_{leg})	$1.28 \times 10^{-3}\Omega$ cm
Thermocouples (or thermoelectric material inside module)	
Number of thermocouples (n)	127
Seebeck coefficient (S_{mat})	$2nS_{leg} = 53.34$ mV/K
Thermal resistance ($R_{th,mat}$)	$1/2nK_{leg}G_{leg} = 2.234$ K/W
Electric resistance ($R_{el,mat}$)	$2nR_{leg}/G_{leg} = 2.858\ \Omega$
Figure of merit (ZT)	$S^2_{mat}/(R_{el,mat}/R_{th,mat}) = 0.77$

EXPERIMENTAL SETUP

The experiment was performed on the roof top of the Solar Energy Lab, Mechanical Engineering Department, NED University, Karachi (24.933°N, 67.111°E), Pakistan. All the experimental measurements were taken from a data-logging system (DLS) directly connected to the prototype (Fig. 6a), and a nearby weather-monitoring system (WMS; Fig. 6b). The observations from both systems were synchronized using a real-time clock (RTC). The DLS consisted of a Genuino UNO and a Genuino Mega 2560, which are open-source, programmable, prototyping hardware boards. A data-logging shield, compatible with Genuino UNO, along with an 8-gigabyte secure digital (SD) card, was mounted on the Genuino UNO. However, all the sensors were attached to the Genuino Mega 2560 because it had sufficient analog-in pins to accommodate all sensors. The Genuino Mega 2560 was programmed to continuously exchange readings from sensors with the Genuino UNO through serial communication (TX-RX). The Genuino UNO was programmed to store incoming data along with a date/time stamp by appending it in a computer file with a comma-separated value (CSV) format, every 30 s. Nine precision centigrade temperature sensors (LM35, Texas Instruments) were used, of which eight were adhered on both sides of the module, while the remaining one was suspended for sensing ambient temperatures (Fig. 6c). All the modules were

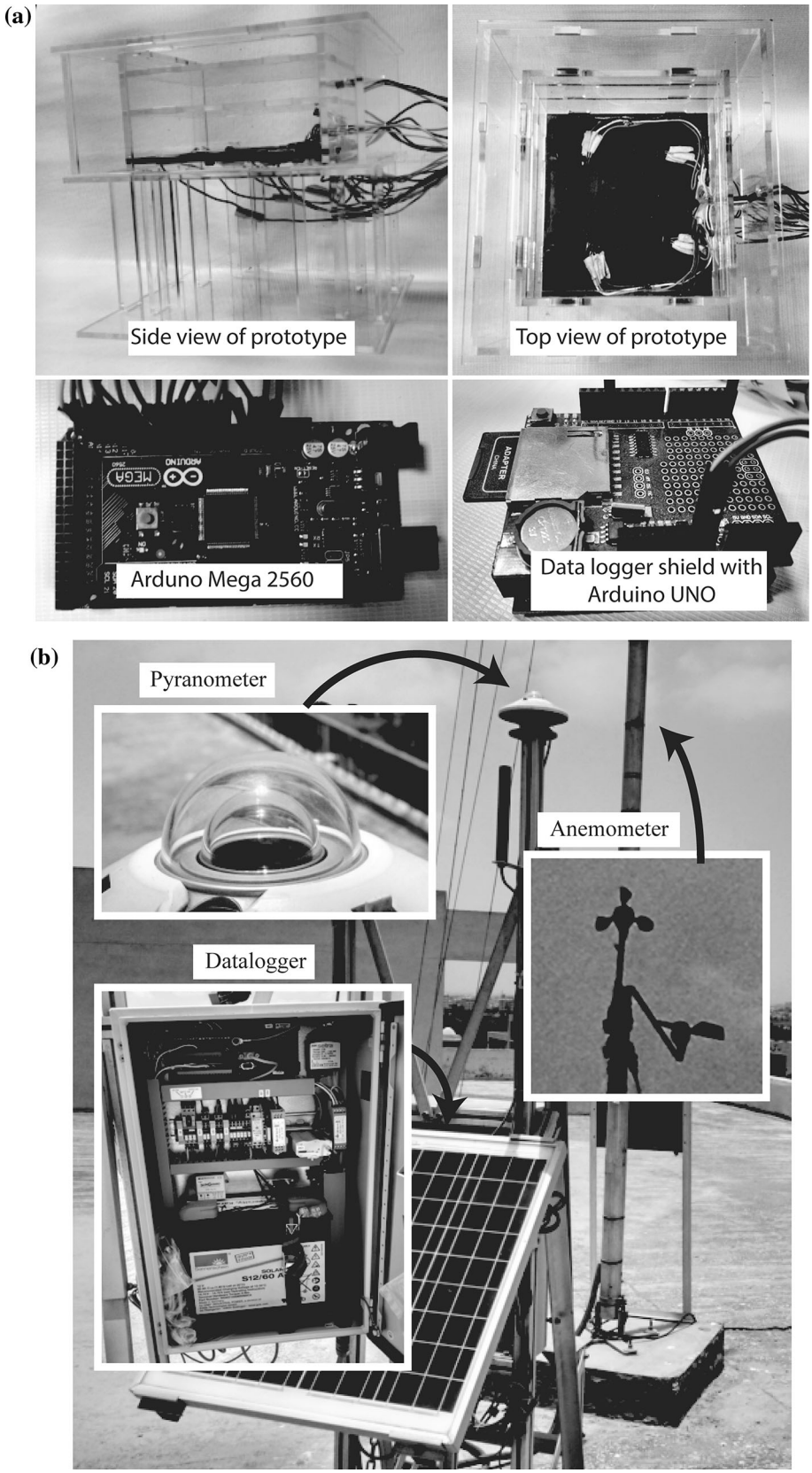

Fig. 6. (a) Data-logging system (DLS) directly connected to the prototype. (b) Weather-monitoring system (WMS) located on roof of a nearby building. (c) Schematic diagram showing prototype connections with DLS.

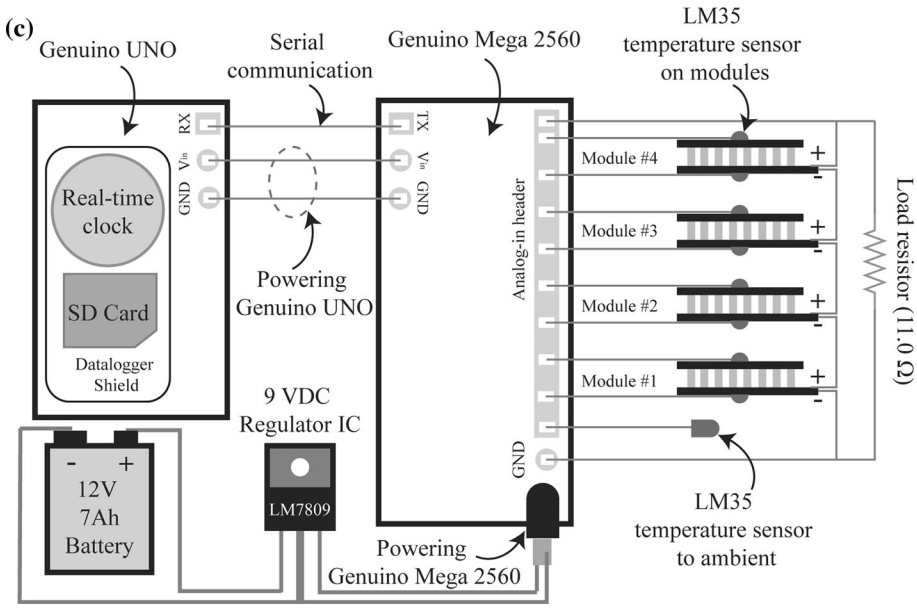

Fig. 6. continued.

connected in series along with a fixed temperature-independent resistor (11.0 Ω), which served as the electric load. The voltage drop across this resistor was also recorded. The Genuino Mega 2560 was powered by a 12-V (7-Ah) battery regulated to 9 V using an LM7809 integrated circuit to ensure stable power supply. The Genuino UNO was powered from the V_{in} pin of the Genuino Mega 2560. Built-in RTC inside the data-logging shield was carefully synchronized with the local time. At WMS, solar radiation on the horizontal and wind speeds were monitored using a CMP11 pyranometer (Kipp & Zonnen) and a 40H anemometer (NRG Systems), respectively. WMS was also synchronized with local time. A manual bubble level was used to ensure horizontal placement of the prototype on the ground. Measurements were taken during peak hours on a clear day in the month of May. The chosen location was absolutely free of shadows of nearby obstacles during measurements. The DLS circuit was also placed well away from the prototype to avoid shadowing the prototype.

RESULTS AND DISCUSSIONS

Measurements

After the prototype became thermally stable, 140 observations were carefully recorded. The ambient temperatures, module temperatures and load voltages are presented in Fig. 7. The hot-side temperature, cold-side temperature and their difference in a particular observation is represented by a mean corresponding temperature of all modules (e.g. the hot-side temperature shown is $(T_{h_1} + T_{h_2} + T_{h_3} + T_{h_4})/4$). The averages of all hot-side and cold-side temperatures were found to be 66.2 ± 4.6°C and 58.1 ± 2.3°C, respectively. The percentage difference between hot-side temperatures of individual modules compared to the average temperature was around ± 3.8%, which was smaller than the difference at the cold sides (± 5.3%). One main reason for this relatively higher difference is the inherent PTR, which may be different for each module. For all observations, the temperature differences and corresponding load voltages were found to be 8.1 ± 20%°C and 180 ± 17% mV, respectively. Moreover, the trends in these temperature differences and load voltages were similar. This was expected from Eq. 5. The ambient temperature at the site's location, solar radiation on the horizontal surface and wind speeds were around 32 ± 5%°C, 600–650 W/m^2 and 4–5 m/s, respectively.

Simulation Parameters

The first step when setting up simulation parameters is to determine the PTR of every module. The same prototype can be used, but the modules should be connected individually to DLS (not in series) in the absence of an electric load.

Experiments were performed with the above system and PTR was evaluated using the methodology explained earlier. Figure 8 shows the histograms of PTR for each module, while their mean values and standard deviations are listed in Table - II. In later sections, only the mean values of PTR are considered for simulation purposes.

The next step is to determine U_{loss}, which depends entirely upon the thermal design of the prototype. For this, we consider a thermal network containing all the resistances (K m^2/W) that account for these losses, as shown in Fig. 9. It is assumed that the heat transfer takes place in one direction and that

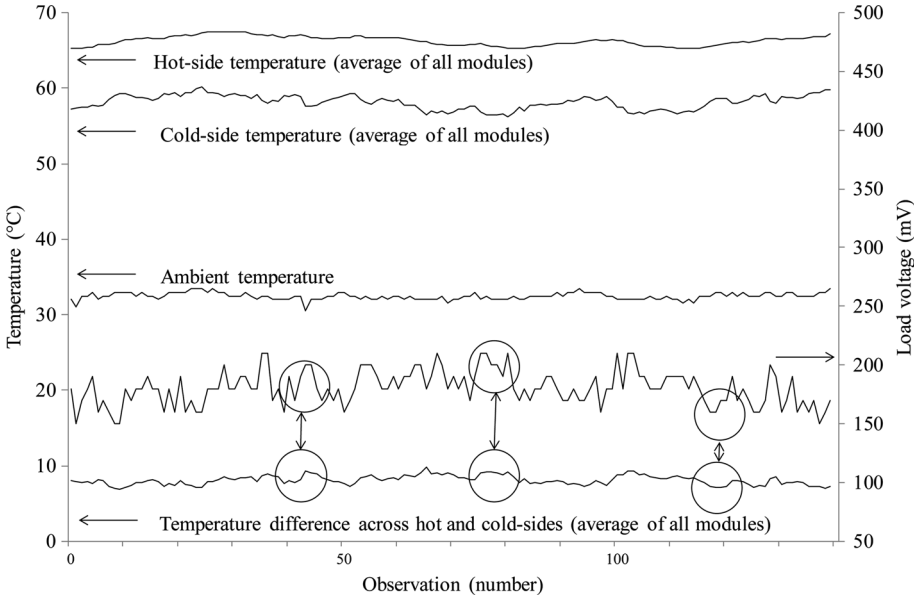

Fig. 7. Ambient temperatures, hot-side and cold-side temperatures, their differences, and corresponding load voltage recorded during the experiment. Values associated with modules are shown as an average value of all modules at a particular observation. Similarity between the trends of temperature difference across module surfaces and load voltage is also evident.

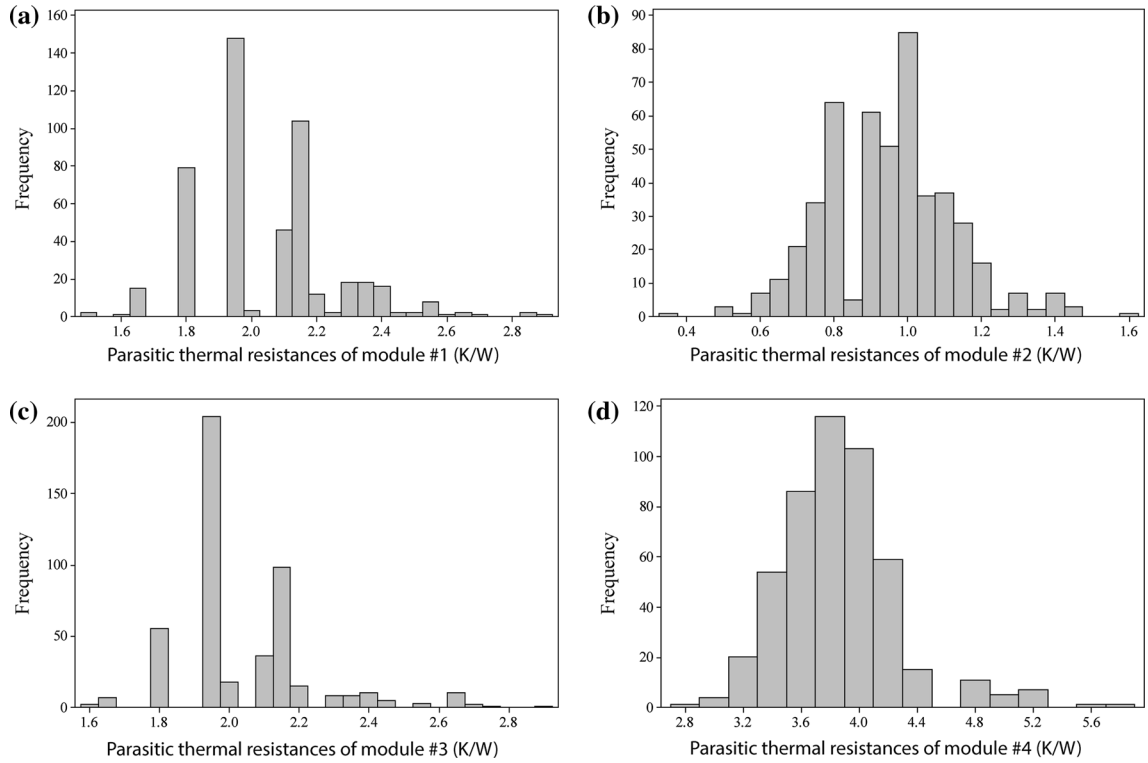

Fig. 8. Histograms of experimentally evaluated parasitic thermal resistances of each module: (a) $R_{th,par}$ for module #1 (K/W), (b) $R_{th,par}$ for module #2 (K/W), (c) $R_{th,par}$ for module #3 (K/W), and (d) $R_{th,par}$ for module #4 (K/W).

all the losses are from the top side, which consists of (starting from modules) an air-tight chamber, an acrylic sheet, another air-tight chamber and acrylic sheet and finally wind convection.

U_{loss} can, therefore, be calculated as:

$$U_{loss} = \left(\frac{1}{h_{nc}} + \frac{t_{acr}}{k_{acr}} + \frac{1}{h_{nc}} + \frac{1}{h_w}\right)^{-1} \quad (18)$$

Table II. Means and standard deviations of experimentally evaluated parasitic thermal resistances of each module

Module	1	2	3	4
PTR (mean, W/K)	2.05	0.95	2.04	3.89
PTR (standard deviation, W/K)	0.22	0.17	0.19	0.41

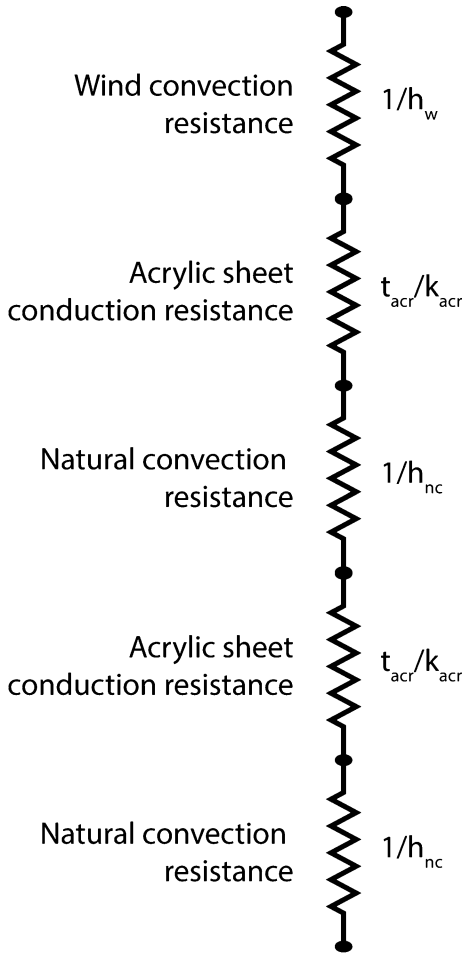

Fig. 9. All the resistances that contribute to the thermal loss coefficient of the prototype. It is assumed that the losses occur only from the top side of the prototype, which consists of an air-tight chamber, an acrylic sheet, another air-tight chamber and acrylic sheet and finally wind convection.

where h_{nc} (W/m^2 K) is the natural convection coefficient inside the chamber (and in the space above chamber), and t_{cr} (mm) and k_{cr} (W/mK) are the thickness and thermal conductivity of the acrylic sheets, respectively. Assuming $h_{nc} = 5.0$ W/m^2 K,[26] $k_{cr} = 0.2$ W/mK[27] and taking $t_{cr} = 4.0$ mm, U_{loss} at an average wind speed of 4.0 m/s was evaluated as approximately 2.0 W/m^2 K.

For simulation purposes, the technical specifications of modules were taken from Table I and other necessary parameters were taken from the "Measurements" section.

Model Validation

The established model was solved for two solar intensities: 600 W/m^2 and 650 W/m^2. These were the extreme values observed during the experiment. Table III lists the simulation means of the averages of all modules' hot-side and cold-side temperatures and load voltages as 63.13°C, 57.17°C and 200 mV, respectively. The model results were in good agreement with experimental outcomes because the differences between their means were within the spans reported during experiments. Thus, the established analytical model can confidently be used for predicting the load voltages, power outputs and efficiency of an ASFTEG. The mean power output and efficiency of the ASFTEG at a given electric load were found to be 3546 μW and 0.08%, respectively.

System Optimization

In this section, the established analytical model is used to determine ways to maximize power output and overall conversion efficiency of an ASFTEG by optimizing the thermal and electrical designs.

Optimizing Thermal Design

The performance of a thermal design is strongly influenced by the U_{loss} coefficient. To evaluate its impact on the overall performance of an ASFTEG, the analytical model was simulated with different values of U_{loss}, taking solar intensities between 300 W/m^2 and 1000 W/m^2, while the rest of the parameters were set as discussed in the "Simulation Parameters" section. Simulated power outputs and overall efficiencies are shown in Figs. 10 and 11, respectively. Curves 1–4 in these figures represent ideal thermal design, the prototype design fabricated for this work, and two poor designs, respectively. Figure 10 shows that an ideal design (having no heat losses, i.e. $U_{loss} = 0$ W/m^{2}K) would produce the maximum power output. At the highest solar intensity of 1000 W/m^2, the power output from the ASFTEG would be 10642 μW. However, at the same level of solar intensity, a poor thermal design ($U_{loss} = 6.0$ W/m^{2}K) would reduce the output to only 6220 μW. Also, the difference between all power output curves, which eventually dictate performance loss, was found to increase proportionally with the solar intensity. The highest differences (hence, losses) between curves 1–2, 2–3 and 3–4 were at a 1000-W/m^2 solar intensity, which were 1890 μW, 1427 μW and 1105 μW, respectively.

Table III. Results of the established analytical model when simulated at 600-W/m^2 and 650-W/m^2 solar intensities

	Average hot-side temperature of all modules (°C)	Average cold-side temperature of all modules (°C)	Load voltage (mV)
Model prediction (at G = 600 W/m^2)	61.96	56.16	190
Model prediction (at G = 650 W/m^2)	64.43	58.17	210
Model prediction (mean)	63.19	57.17	200
Mean experimental observations along with span	66.20 ± 4.6%	58.10 ± 8.3%	180 ± 17%

The model was in good agreement with the experimental observations.

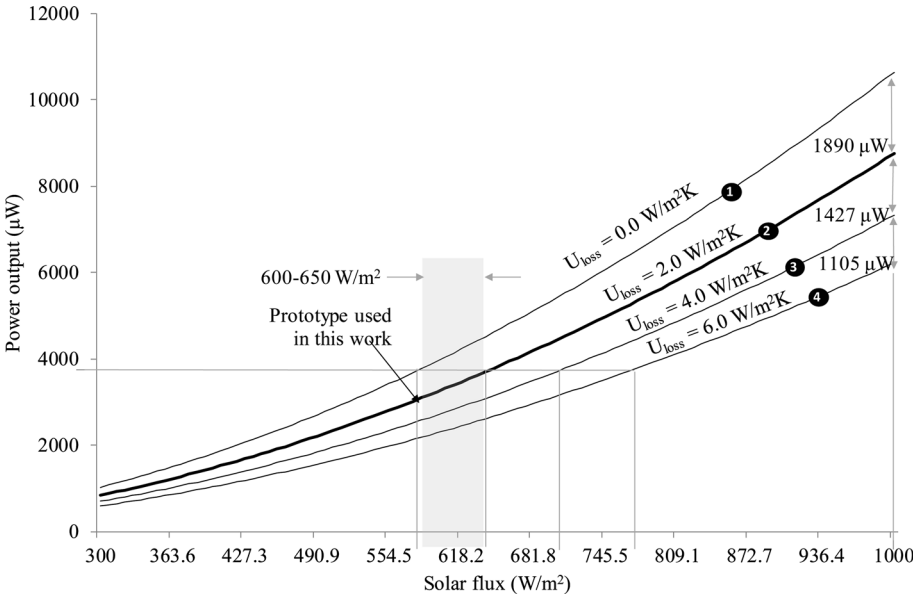

Fig. 10. Power output of an ASFTEG at different values of U_{loss} coefficient.

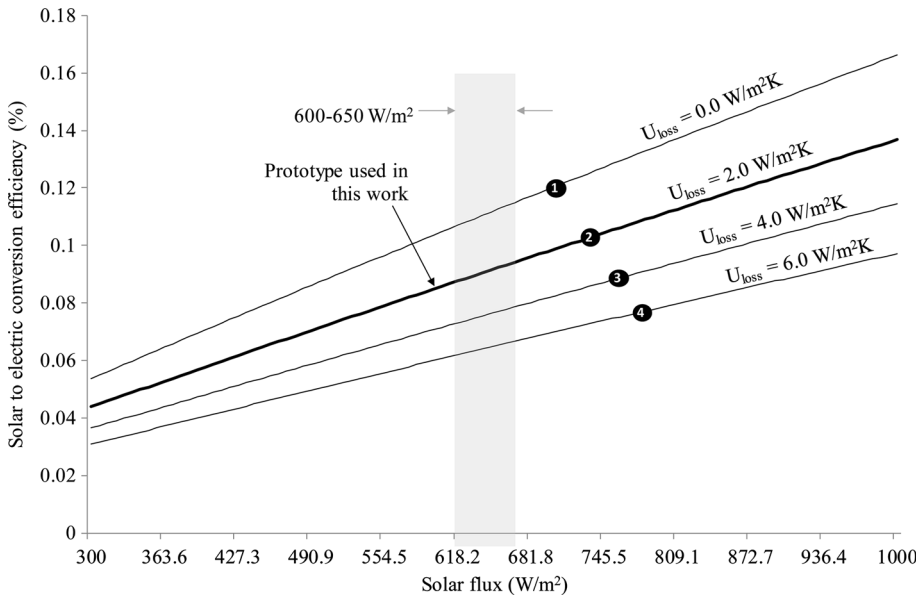

Fig. 11. Solar-to-electric conversion efficiencies of an ASFTEG at different values of U_{loss} coefficient.

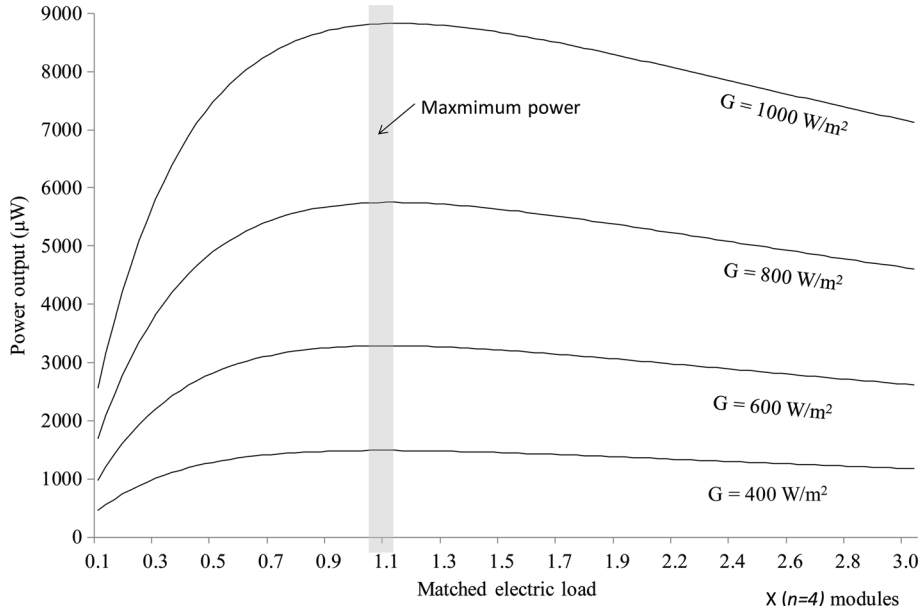

Fig. 12. Power output of an ASFTEG at different values of matched electric load.

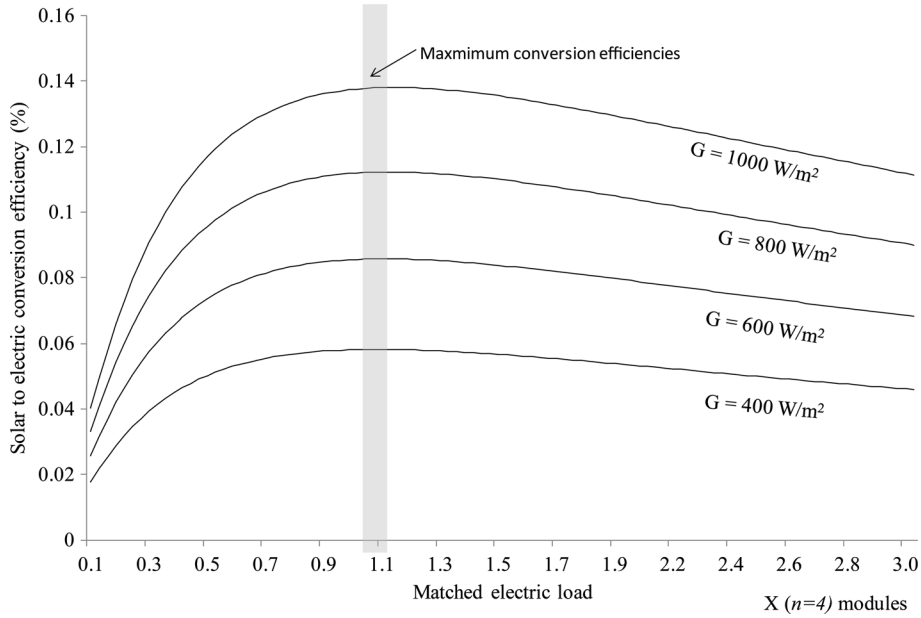

Fig. 13. Solar-to-electric conversion efficiency of an ASFTEG at different values of matched electric load.

Alternatively, it can be inferred that having good thermal design could be advantageous in producing power at even lower solar intensities. For example, 4000 μW can be produced through an ideal thermal design at a solar intensity of only 600 W/m^2, while to generate the same output, a solar intensity of more than 880 W/m^2 would be required in a poor thermal design. This may considerably affect day-round generation because high solar intensities are generally less frequent.

Solar-to-electric conversion efficiencies corresponding to the above-mentioned designs are depicted in Fig. 11. These curves are quite consistent with those shown in Fig. 10 and it can again be seen that higher conversion efficiencies can be achieved with good thermal designs. The highest overall conversion efficiencies of 0.17%, 0.14%, 0.11%, and 0.08% were achieved in an ideal design, the prototype design and in two poor designs, respectively.

This study indicates that a good thermal design with a low loss coefficient can yield high power outputs and overall efficiencies, even at lower solar radiation levels. Some suggestions for achieving a low U_{loss} value in an ASFTEG include the use of evacuation techniques and making chambers with materials showing good solar transmittance and poor thermal conductivity.

Optimizing Matched Electric Load

The established analytical model was simulated with different values of matched electric load (M) to determine its effect on power output and overall conversion efficiency. The results are shown in Figs. 12 and 13, respectively. Simulation parameters other than the matched electric load were kept constant, as discussed in the "Simulation Parameters" section.

Figure 12 shows that a strong impact of matched load on power output was found at high solar intensities. The power output reached 8832 μW at a matched load of 4.62 (= 1.155 × 4 number of modules) when the solar intensity was 1000 W/m^2. At the same level of solar intensity, power output dropped by 30% to 2568 μW at a matched load of 0.4. Looking at all levels of solar intensities, the power outputs were highest for matched loads between 1.0 and 1.15 times the number of modules. At a lower value of matched load, the slope of the power output is steeper, which means that even a slight mismatch may result in exceptionally low performance. However, beyond this value, the power output reduces with a gentle slope.

The results for solar-to-electric conversion efficiency in Fig. 13 are similar to those for power outputs. The highest overall conversion efficiency of 0.14% was obtained at a solar intensity of 1000 W/m^2 with a matched load of around 1.1 times the number of modules. At the same level of solar intensity, the efficiency can drop to only 0.04%, which is less than 30% of maximum efficiency. Also, the drop in efficiency is significant when the matched load is less than 1.0 × modules, whereas it is comparatively less affected beyond this value.

An optimized matched load of 1.0 × modules or above is recommended for maximum power outputs and conversion efficiencies during the operation of ASFTEGs in solar intensities up to 700 W/m^2. At higher solar intensities, the matched load should be held close to 1.0 × modules. Using a matched load of less than 1.0 is strongly discouraged.

CONCLUSIONS

An analytical model for predicting performance parameters, including load voltage, power output and overall solar-to-electrical conversion efficiency for an ASFTEG in closed-circuit operation mode has been established. The model considers individual temperature variations across each module in the array. Also, the proposed model is more practical since it is based on energy balances, which allow for incident solar radiation, thermal losses, energy transfer through modules, electric power conversion and waste heat rejection. The inherited parasitic thermal losses of individual modules are also incorporated in the model, which makes it more realistic. With the given set of simulation parameters, an ASFTEG consisting of four commercially available Bi_2Te_3 modules had a predicted load voltage of 200 mV, generating 3546 μW electric power output with 0.08% overall conversion efficiency. These predictions were found to be in good agreement with experimental observations taken from a prototype ASFTEG which was developed for validation purposes. Later, the model was simulated to maximize performance by optimizing the thermal and electrical design of the ASFTEG. This simulation concluded that:

1. An ASFTEG with good thermal design (having a low U_{loss} value) will perform much better, even at low solar intensities.
2. Enhanced performance can be achieved with good thermal designs at high solar intensities.
3. Electrical matched load (M) has a strong influence on the overall performance of an ASFTEG.
4. For the best performance, a matched electrical load of 1.0 × modules (or slightly higher) is suggested when the solar intensities are up to 700 W/m^2.
5. At high solar intensities, the optimum matched electrical load is 1.0.
6. An electrical matched load of less than 1.0 is not recommended at any solar intensity.

Beyond the current limitations associated with improvement in thermoelectric materials, this study will eventually lead to the successful development of portable roof-top renewable TEGs.

REFERENCES

1. N.U. Rehman and M.A. Siddiqui, *J. Renew. Sustain. Energy* (2015). https://doi.org/10.1063/1.4921386.
2. N.U. Rehman and M.A. Siddiqui, *J. Electron. Mater.* (2016). https://doi.org/10.1007/s11664-016-4689-9.
3. N.U. Rehman and M. Siddiqui, *J. Electron. Mater.* (2016). https://doi.org/10.1007/s11664-016-5230-x.
4. D. Mills, *Sol. Energy* (2004). https://doi.org/10.1016/S0038-092X(03)00102-6.
5. H. Xi, L. Luo, and G. Fraisse, *Renew. Sustain. Energy Rev.* (2007). https://doi.org/10.1016/j.rser.2005.06.008.
6. D.M. Rowe, *Thermoelectrics Handbook* (Boca Raton: CRC Press, 2006), pp. 1–4.
7. A. Agbossou, Q. Zhang, G. Sebald, and D. Guyomar, *Sens. Actuators A Phys.* (2010). https://doi.org/10.1016/j.sna.2010.06.026.
8. M.A. Karri, E.F. Thacher, and B.T. Helenbrook, *Energy Convers. Manag.* (2011). https://doi.org/10.1016/j.enconman.2010.10.013.
9. R. Amatya and R.J. Ram, *J. Electron. Mater.* (2010). https://doi.org/10.1007/s11664-010-1190-8.
10. S.A. Omer and D.G. Infield, *Energy Convers. Manag.* (2000). https://doi.org/10.1016/S0196-8904(99)00134-X.
11. B. Orr, J. Taglieri, L.C. Ding, and A. Akbarzadeh, *Energy Convers. Manag.* (2016). https://doi.org/10.1016/j.enconman.2016.02.074.

12. M.H. Nia, A.A. Nejad, A.M. Goudarzi, M. Valizadeh, and P. Samadian, *Energy Convers. Manag.* (2014). https://doi.org/10.1016/j.enconman.2014.04.041.
13. D. Kraemer, K. McEnaney, M. Chiesa, and G. Chen, *Sol. Energy* (2012). https://doi.org/10.1016/j.solener.2012.01.025.
14. H.J. Goldsmid, J.E. Giutronich, and M.M. Kaila, *Sol. Energy* (1980). https://doi.org/10.1016/0038-092X(80)90311-4.
15. S.A. Omer and D.G. Infield, *Sol. Energy Mater. Sol. Cells* (1998). https://doi.org/10.1016/S0927-0248(98)00008-7.
16. B. Lenoir, A. Dauscher, P. Poinas, H. Scherrer, and L. Vikhor, *Appl. Therm. Eng.* (2003). https://doi.org/10.1016/S1359-4311(03)00065-6.
17. A. Montecucco, J. Siviter, and A.R. Knox, *Appl. Energy* (2014). https://doi.org/10.1016/j.apenergy.2014.02.030.
18. A. Vargas-Almeida, M.A. Olivares-Robles, and P. Camacho-Medina, *Entropy* (2013). https://doi.org/10.3390/e15062162.
19. A. Vargas-Almeida, M.A. Olivares-Robles, and F.M. Lavielle, *Entropy* (2015). https://doi.org/10.3390/e17117387.
20. C.T. Hsu, G.Y. Huang, H.S. Chu, B. Yu, and D.J. Yao, *Appl. Energy* (2011). https://doi.org/10.1016/j.apenergy.2011.07.033.
21. D. Ebling, K. Bartholomé, M. Bartel, and M. Jägle, *J. Electron. Mater.* (2010). https://doi.org/10.1007/s11664-010-1331-0.
22. Y. Apertet, H. Ouerdane, O. Glavatskaya, C. Goupil, and P. Lecoeur, *EPL* (2012). https://doi.org/10.1209/0295-5075/97/28001.
23. W.H. McAdams, *Heat Transmission*, 3rd ed. (New York: McGraw-Hill, 1954), p. 249.
24. T.L. Bergman, F.P. Incropera, and A.S. Lavine, *Fundamentals of Heat and Mass Transfer*, 6th ed. (New York: Wiley, 2007), pp. 3–6.
25. S.B. Riffat, X. Zhao, and P.S. Doherty, *Appl. Therm. Eng.* (2005). https://doi.org/10.1016/j.applthermaleng.2004.08.010.
26. Y. Cai, J. Xiao, W. Zhao, X. Tang, and Q. Zhang, *J. Electron. Mater.* (2011). https://doi.org/10.1007/s11664-011-1616-y.
27. Kaysons Akrylic furniture & accessories. http://www.builditsolar.com/References/Glazing/physicalpropertiesAcrylic.pdf. Accessed 21 Mar 2018.